*Materials Transactions*, Vol. 65, No. 7 (2024) pp. 780 to 789

# Invasion/Permeation Hydrogen in Cathodic Charged SUS316 Columnar Crystals Evaluated with a Scanning Kelvin Probe Force Microscope

Yoshiharu Murase* and Hideki Katayama

*National Institute for Materials Science, Tsukuba 305-0047, Japan*

The monitoring of invasion/permeation hydrogen on entry/exit surfaces of cathodically charged SUS316 columnar crystals was conducted with a scanning Kelvin probe force microscope (SKPFM) under atmospheric pressure. Columnar crystal specimens covered with oxide films on their surfaces under room conditions were prepared for cathodic charging tests and subsequent SKPFM measurements. The invaded hydrogen on the entry surface was detected at the δ-ferrite phases for 7 d after charging, and the segregation of invaded hydrogen at the boundaries between the δ-ferrite and austenite matrix was prolonged for >10 d after charging. The permeated hydrogen on the exit surface was detected at the δ-ferrite phases for 3 d after charging, but was not substantial at some of the δ-ferrite phases regardless of the charging. Segregation of permeated hydrogen at the boundaries between the δ-ferrite and some of the intermetallic precipitates was prolonged for 7 d after charging. The behaviors of invaded/permeated hydrogen based on heterogeneous microstructures are discussed to improve understanding of the hydrogen embrittlement mechanism in weld metals. [doi:10.2320/matertrans.MT-M2024009]

(Received January 25, 2024; Accepted April 8, 2024; Published April 19, 2024)

**Keywords:** *hydrogen monitoring, scanning Kelvin probe force microscope, columnar crystal, delta ferrite, secondary intermetallic phase*

## 1. Introduction

Hydrogen is a next-generation clean energy for reducing the environmental burden caused by using fossil fuels; extensive research and development have been carried out on hydrogen infrastructure materials for realization of a hydrogen-based society. Hydrogen embrittlement (HE) induced by hydrogen invading from the surface of metallic materials—leading to a decrease in strength and ductility—is an important issue in the context of research and development of structural materials with excellent safety, reliability, and economic efficiency. Austenitic stainless steels are highly resistant to HE and retain substantial ductility when exposed to hydrogen compared with other types of steels [1, 2]. However, during welding (indispensable for constructing hydrogen-related facilities), a dendrite structure—consisting of δ-ferrite and secondary phases such as intermetallic precipitates in the austenitic (γ) matrix—is formed during solidification of welded metals for austenitic stainless steels. Fracture mechanisms of hydrogen precharged welds of austenitic stainless steels are different from those of base materials, and it has been reported that δ-ferrite phases as well as their boundaries in the dendrite structure facilitate initiation and propagation of microcracks in tensile tests [1, 3]. Some of the intermetallic precipitates that form in weld metals have also been reported to be susceptible to HE in terms of their intrinsic brittleness and the changes in the local elemental distribution [4]. To further understand the HE mechanism in weld metals, applying an innovative experimental method might be helpful to clarify hydrogen behavior based on the heterogeneous microstructures in the dendrite structure.

Scanning Kelvin probe force microscopy (SKPFM) [5–7] is a powerful tool for mapping the hydrogen distribution in materials; it has a spatial resolution of up to several tens of nanometers and detects surface potential changes that are pertinent to diffusible hydrogen on the metal surface [8, 9]. This technique also enables sequential kinetic analysis of the hydrogen distribution with continuous measurements [9]. However, SKPFM cannot evaluate the local hydrogen concentration from the absolute value of the surface potential obtained from the measurement because of the absence of a calibrated reference electrode [9]. Namely, the potential value is considered as relative, and the mapping data of potential contrast in the scanned area are pertinent to subsequent experimental evaluation. When performing SKPFM measurements of steel materials under atmospheric pressure, the surface potential changes because of formation and growth of oxide films. In particular, local elemental concentration gradients in heterogeneous microstructures give rise to local potential contrasts because of the differences in the stability of the passive oxide film [10, 11]. Even in steel materials covered with an oxide film on their surfaces, hydrogen can be detected because hydrogen reduces Fe(III) to Fe(II) in the oxide film, leading to a change of the surface potential of the oxide film [12, 13]. Therefore, when detecting hydrogen in steel materials by SKPFM under atmospheric pressure, it is necessary to determine whether the change in surface potential is because of hydrogen or the oxide film. Some literature [14, 15] has reported the hydrogen distribution and its time-dependence on the entry surface of precharged maraging stainless steels with SKPFM under atmospheric pressure. However, detecting permeated hydrogen at the exit surface has not been conducted for precharged steels when covered with oxide films, but is expected to further advance understanding of the HE mechanism (pertinent to the behavior of diffusible hydrogen). Coating a metal surface with a thin Pd film can substantially improve the hydrogen detection efficiency up to several parts per billion by preventing oxide film formation and hydrogen escape from the metal surface [9]. Sophisticated analyses of the permeated hydrogen behavior for cathodically charged stainless steels have been conducted by SKPFM measurements on Pd-coated exit surfaces [16, 17]. However, some local limitations of the hydrogen diffusion because of the interaction with oxide films on the surface [18] are pertinent to the HE mechanism

---

*Corresponding author, E-mail: yoshiharu@nims.go.jp

in practical contexts. Therefore, it is pertinent to accumulate sufficient data of hydrogen monitoring for steel materials, with and without a Pd coating on their surfaces.

In the present study, the time-sequential distribution of the surface potential on the entry/exit surfaces of cathodically charged SUS316 columnar crystal specimens was evaluated by SKPFM under atmospheric pressure. Because the columnar structure is one of the main structures of weld metals, columnar crystal specimens covered with oxide films on the surfaces were prepared as a first step in evaluating the HE mechanism in weld metals used in practical conditions. The microstructures of the entry/exit surfaces were also evaluated by electron backscattered diffraction (EBSD) and energy-dispersive X-ray spectroscopy (EDS) in the same areas of the SKPFM measurements. The purpose of the present study was to monitor the behavior of invaded/permeated hydrogen based on the heterogeneous microstructures in order to improve our understanding of the HE mechanism in weld metals.

## 2. Experimental Procedure

A commercial SUS316 was used for fabricating columnar crystals. Table 1 shows the chemical composition of SUS316. Fragments of SUS316 were enveloped in a crucible and heated at 1823 K, followed by unidirectional solidification in a furnace at a pulling speed of 200 mm/h to fabricate an ingot of SUS316 columnar crystal. Figure 1 shows a schematic of specimen preparation as well as microstructural images of a cross section and the specimen surface. The ingot was sliced to plate across the columnar crystal structure [Fig. 1(a)], and a disc with a diameter of 20 mm as well as a cross-sectional plate was cut out from the plate [Fig. 1(b)] with an electric discharge machine. The disk and cross-sectional plate were ground to a thickness of 0.3 mm, mechanically polished with #800 and #1200 emery paper for 30 min, and mirror-finished with a colloidal silica suspension (grain size of 0.04 μm) for 1 h to form a specimen [Fig. 1(b) and (c)]. Laser markings were introduced onto the specimen surface as guides for multimodal (SKPFM, EBSD, and EDS) measurements. EBSD measurements were performed on the specimen surface as well as a cross-sectional plate with a scanning electron microscope (HITACHI-SU5000) equipped with a diffraction detector (APEX, Velocity EBSD camera). Figure 1(d), (e) shows typical microstructural images of the inverse pole figure (IPF) map and enlarged phase map, respectively, on a cross-sectional plate; and Fig. 1(f), (g) shows images of the IPF and the enlarged phase maps, respectively, on the specimen surface. In the unidirectional solidification process, austenite (γ) and adjacent δ-ferrite grow along their respective preferential crystal orientations, and the adjacent δ-ferrite grows continuously when a single austenite grows continuously [19]. However, when austenite newly nucleates or diminishes during the process, a continuous growth of the adjacent δ-ferrite is also interrupted. Therefore, some of δ-ferrite phases are discontinuous inside specimen [Fig. 1(e)]. EDS measurements were performed on the specimen surface with a scanning electron microscope (HITACHI-SU5000) equipped with an X-ray detector (APEX, Octane Elite). The acceleration voltage was 15 kV, the energy spectrum of the characteristic X-rays was counted as a pulse signal in 10-eV increments in the range 0–20 keV, and measurements were

Table 1 Chemical composition of SUS316 stainless steel (mass percentage).

| Ni | Cr | Mn | Mo | C | Si | P | S | Fe |
|---|---|---|---|---|---|---|---|---|
| 10.30 | 16.79 | 1.17 | 2.16 | 0.06 | 0.68 | 0.027 | 0.001 | balance |

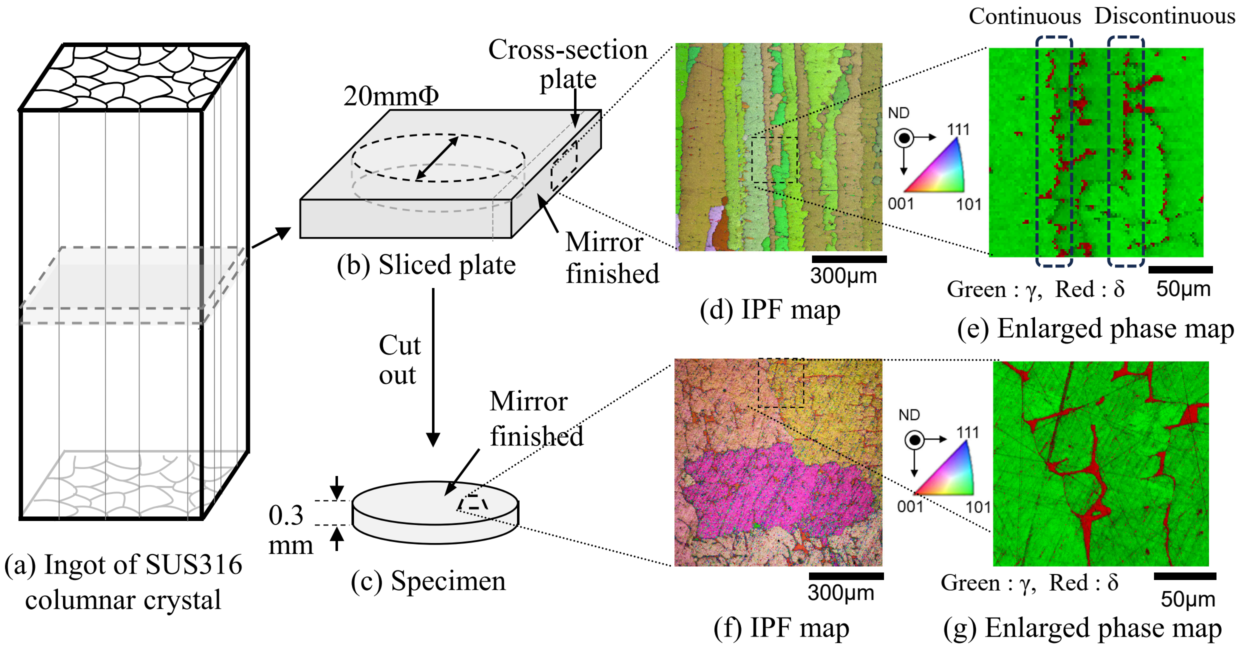

Fig. 1 Schematic of specimen preparation and microstructural images of cross section and specimen surface: (a) Ingot of SUS316 columnar crystal; (b) Sliced plate; (c) Cut out of disk specimen and images of cross section; (d) IPF map and (e) Enlarged phase map, and images of specimen surface; as well as (f) IPF map and (g) Enlarged phase map.

conducted until the total count reached the order of $10^6$ to obtain sufficient spectral detection sensitivity. Regarding the intensity maps consisting of spectral counts for each element, Cr, Mo, and Ni maps are presented in the present experiments. Following EBSD and EDS measurements, Ar-ion milling (Hitachi High-Tech, IM4000Plus) was conducted on the specimen surface for 1 min. The accelerating voltage and current values were 4 kV and 120 µA, respectively, with irradiation angles of 80° with respect to the normal direction of the specimen surface. The SKPFM measurements were performed on the specimen surface on the same areas evaluated by EBSD and EDS measurements for each specimen. The SKPFM used in the present study comprised an atomic force microscope, a Kelvin probe, potential measurement devices, and an X–Y stage system (Hitachi High-Tech, AFM5500). The measurement area was 50 µm × 50 µm with data points of 256 px × 256 px. The resolution of the surface topography and potential was 0.1 nm and 1.0 mV, respectively. The measurements were conducted under room conditions (23°C, $\leq$40% relative humidity) with a conductive Rh-coated Si tip as a Kelvin probe with a resonant frequency of approximately 25 kHz in dual-scan mode. Because the measured value of the potential from this device was the potential difference between the bias-controlled Kelvin probe tip and the ground specimen, the absolute value is semi-quantitative; hence, the potential contrast provides useful information reflecting local modifications of surface properties. In the present experiments, surface potential was defined as the reversed sign of the output value from this device (nulling method), and the obtained potential distribution was drawn as the potential map with the lowest value normalized to zero in the map. Further comprehensive explanations regarding the SKPFM measurements can be found elsewhere [20]. Figure 2 shows a schematic of the cathodic hydrogen charging cell installed on the SKPFM sample stage. Cathodic hydrogen charging was performed on the entry surface of the specimen at room temperature by using 0.1 M NaOH, and the charging current was 0.33 mA/cm$^2$. This charging cell enables SKPFM measurements on the exit surface immediately after charging, without removing the specimen from the cell, by switching the connection from Galvanostat to ground (Fig. 2). SKPFM measurements were performed in area A on the entry surface of the cathodically charged specimen as well as areas B and C on the exit surface of the specimen charged from the back. Regarding SKPFM measurements in area A on the entry surface, the specimen was removed from the cell after charging, washed with distilled water, and dried in a vacuum desiccator for 1 h. The SKPFM measurements on the entry surface were conducted before charging, 3-h charging, and an additional 45-h charging (48-h charging total); followed by 5, 7, and 12 d after charging. The interval between 3-h charging and an additional 45-h charging was 2 h. After the measurement of 48-h charging total, the specimen was stored in a dry desiccator. The SKPFM measurements in areas B and C on the exit surface were conducted before charging, 50-min charging, an additional 100-min charging (150-min charging total), and an additional 30-min charging (180-min charging total); followed by 3 d and 7 d after charging. The interval between charging and additional charging was ca. 2 h, corresponding to the measurement time of SKPFM for the two areas. After SKPFM measurements of 180-min charging total, the specimen was removed from the charging cell and stored in a dry desiccator.

## 3. Results and Discussion

### 3.1 Hydrogen monitoring on the entry surface

Figure 3 shows the following: SEM image (Secondary electron image) [Fig. 3(a)]; phase map [Fig. 3(b)]; topography map along the P–Q line [Fig. 3(c)]; as well as intensity maps along the P–Q lines of Cr, Mo, and Ni [Fig. 3(d)–(f), respectively] in area A on the entry surface. The crystal structure had a dendritic structure [Fig. 3(a) and (b)], in which δ-ferrite phases manifested as branches in the austenitic (γ) matrix, and a line segment P–Q with a length of 20 µm was set across the δ-ferrite phase. In the δ-ferrite phase, an approximately 50-nm higher topography [Fig. 3(c)] and higher intensities of Cr and Mo yet lower intensity of Ni were detected [Fig. 3(d)–(f)]. Figure 4 shows potential maps

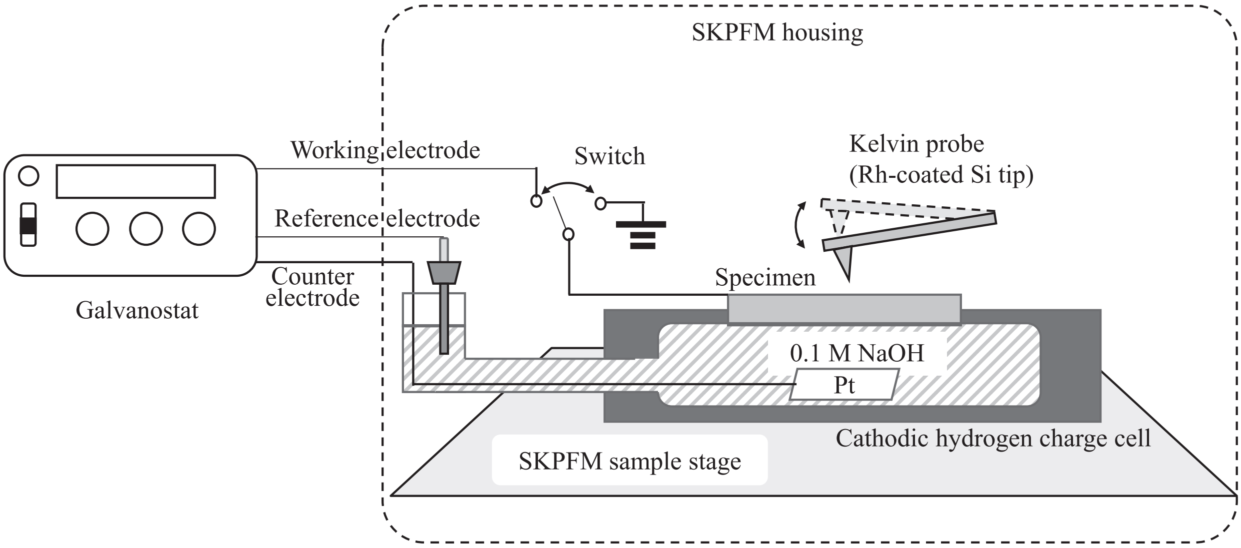

Fig. 2 Schematic of cathodic hydrogen charging cell installed on SKPFM sample stage.

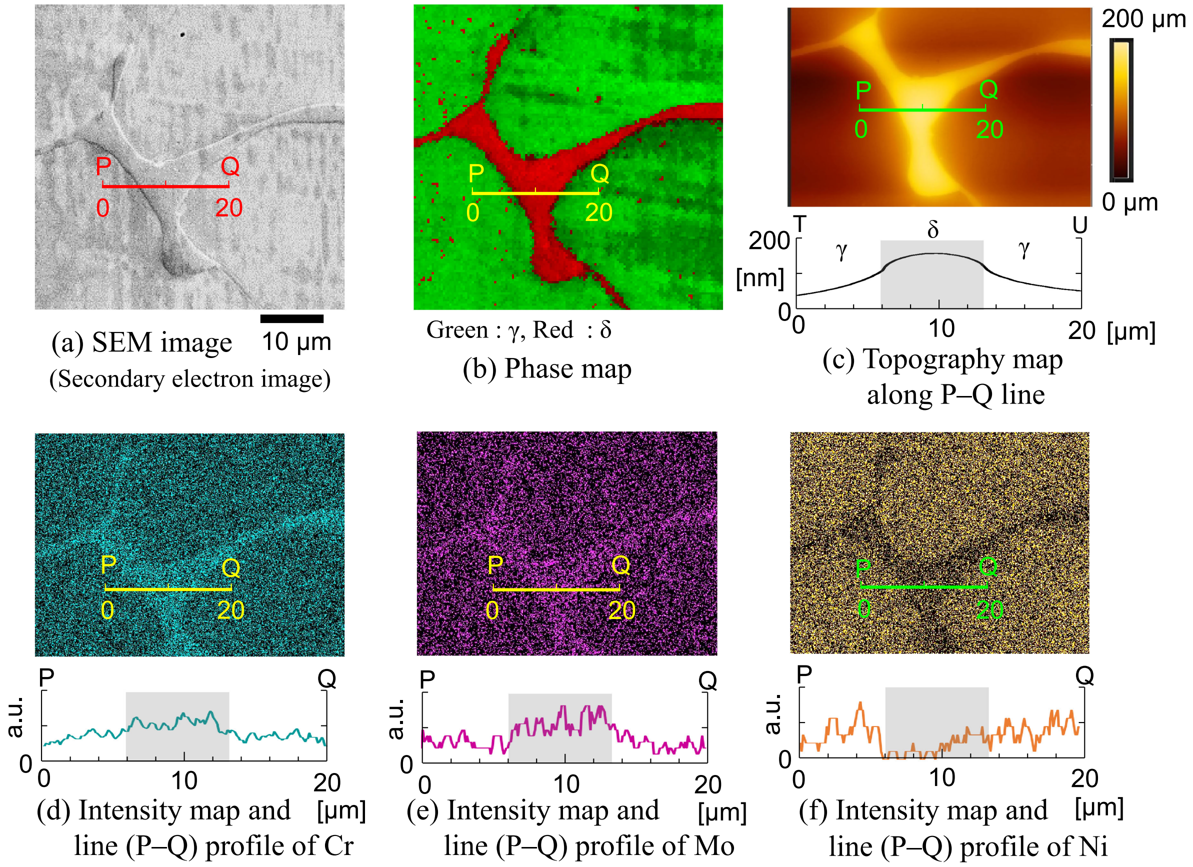

Fig. 3 (a) SEM image; (b) Phase map; (c) Topography map along P–Q line; as well as (d)–(f) Intensity maps along P–Q lines of Cr, Mo, and Ni, respectively, in area A on the entry surface.

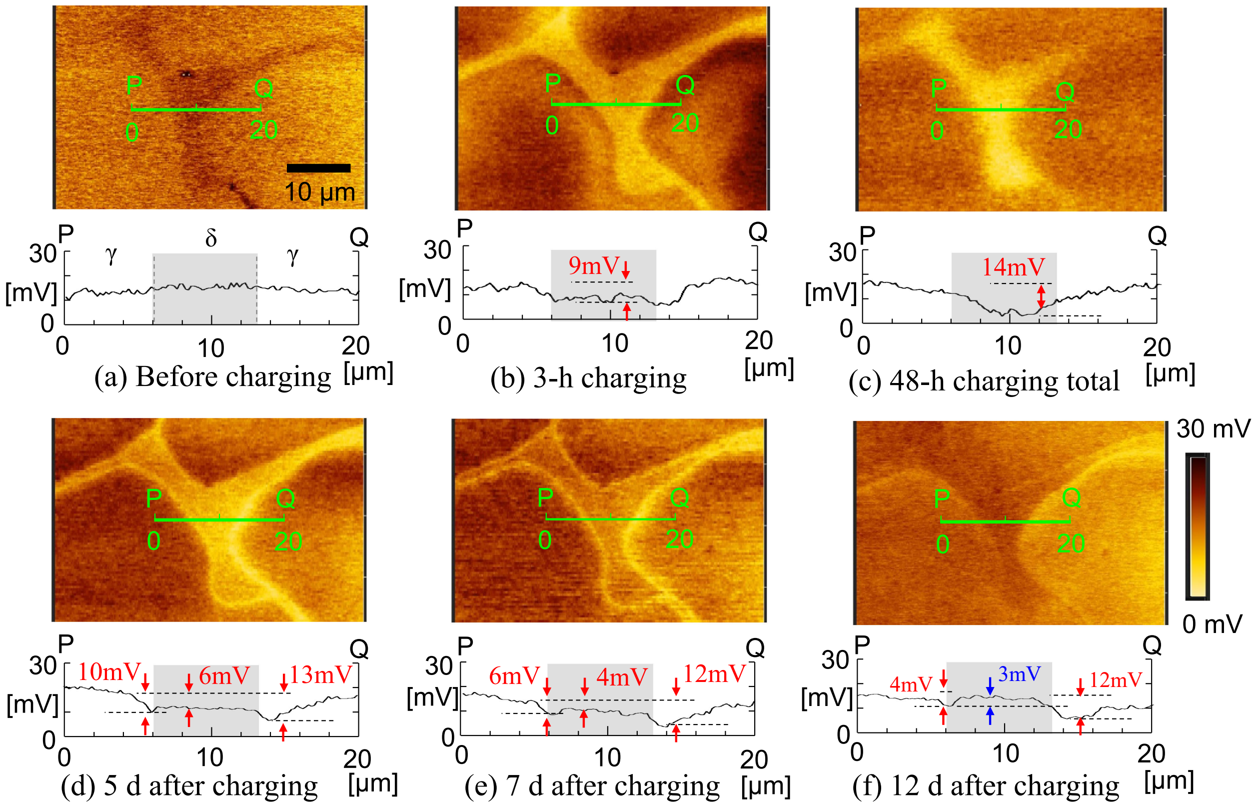

Fig. 4 Potential maps along the P–Q lines in area A: (a) Before charging, (b) 3-h charging, (c) 48-h charging total, (d) 5 d after charging, (e) 7 d after charging, and (f) 12 d after charging.

along the P–Q lines in area A: before charging [Fig. 4(a)], 3-h charging [Fig. 4(b)], 48-h charging total [Fig. 4(c)], 5 d after charging [Fig. 4(d)], 7 d after charging [Fig. 4(e)], and 12 d after charging [Fig. 4(f)]. The potential of the δ-ferrite phase relative to the austenitic (γ) matrix along the P–Q line was almost the same before charging [Fig. 4(a)]; and lower by 9, 14, 6, and 4 mV for 3-h charging [Fig. 4(b)], 48-h charging total [Fig. 4(c)], 5 d [Fig. 4(d)], and 7 d after charging [Fig. 4(e)], respectively, yet higher by 3 mV for 12 d after charging [Fig. 4(f)]. Lower potential at the boundaries of the δ-ferrite phases than that of the austenitic matrix (ranging from 12–13 mV maximum) was detected for 5 d [Fig. 4(d)], 7 d [Fig. 4(e)], and 12 d after charging [Fig. 4(f)].

When SKPFM measurements of steel are conducted under atmospheric pressure, the distribution of the surface potential is influenced by the difference in the stability of the passive oxide film, which depends on the local elemental concentration gradients in the heterogeneous microstructure. Because formation of a passive oxide film was more enhanced in some phases with a higher concentration of Cr or Mo, a clear tendency of a relative increase of the surface potential over time has been reported in such phases [10, 11]. However, a relative decrease of the surface potential in the δ-ferrite phases with higher concentrations of Cr and Mo [Fig. 3(d) and (e)] was detected over time from before to 48-h charging total [Fig. 4(a)–(c)]. Furthermore, the lower potential was gradually recovered in the δ-ferrite phases after charging but prolonged at the boundaries of the δ-ferrite phases, even 12 d after charging [Fig. 4(f)]. Because these series of potential variation over time cannot be explained in terms of forming the passive oxide film, the present authors hypothesize that the diffusion and segregation of invaded hydrogen from cathodic charging [8] would be reflected in the potential variations. Luppo *et al.* [21] confirmed segregation of invaded hydrogen at the boundaries of δ-ferrite phases on the entry surface of a weld metal for cathodically charged austenite stainless steels by hydrogen microprinting. Furthermore, preferential initiation of microcracking at the δ-ferrite phases and propagation of cracks along the boundaries of ferrite phases has been reported in plastic–elastic fracture mechanic tests of precharged weld metals of austenite stainless steels [1, 21]. The present results of SKPFM measurements on the entry surface strongly support the involvement of δ-ferrite phases with hydrogen-assisted cracking of weld metals. Namely, the invaded hydrogen in δ-ferrite phases during charging promptly diffuses and desorbs from the surface, but some of invaded hydrogen preferably segregates at the boundaries even after charging. Thus, monitoring invaded hydrogen in the δ-ferrite phases on the entry surface provides pertinent information on the hydrogen embrittlement mechanism of weld metals. In contrast, the potential changes due to the diffusion of invaded hydrogen in austenite phases would be limited in the present experimental duration (12 d after charging), because the hydrogen diffusion coefficient of the austenite phase is approximately five orders of magnitude smaller than that of the ferrite phase at room temperature [22]. However, since the potential in austenite phases is not considered as a reference potential free from the effect of diffusible hydrogen, the evaluation of the hydrogen concentration in the δ-ferrite phase based on the relative potential with the austenite phase could not be conducted on the entry surface.

### 3.2 Hydrogen monitoring on the exit surface

Figure 5 shows the following: SEM image (Secondary electron image) [Fig. 5(a)]; phase map [Fig. 5(b)]; topography map along the R–S line [Fig. 5(c)]; and intensity maps along the R–S lines of Cr, Mo, and Ni [Fig. 5(d)–(f), respectively] in area B on the exit surface. A line segment R–S with a length of 20 µm was set across the δ-ferrite phase (Fig. 5). In the δ-ferrite phase, an approximately 50-nm higher topography [Fig. 5(c)] and higher intensities of Cr and Mo—yet a lower intensity of Ni—were detected [Fig. 5(d)–(f)]. Figure 6 shows potential maps along the R–S lines in area B: before charging [Fig. 6(a)], 50-min charging [Fig. 6(b)], 150-min charging total [Fig. 6(c)], 180-min charging total [Fig. 6(d)], 3 d after charging [Fig. 6(e)], and 7 d after charging [Fig. 6(f)]. The relative potential of the δ-ferrite phase to the austenite (γ) matrix along the R–S line was almost the same before charging [Fig. 6(a)]; and lower by 3, 5, 4, and 2 mV for 50-min charging [Fig. 6(b)], 150 min total [Fig. 6(c)], 180 min total [Fig. 6(d)], and 3 d after charging [Fig. 6(e)], respectively, yet higher by 3 mV for 7 d after charging [Fig. 6(f)].

The relative decrease and gradual recovery of the surface potential in the δ-ferrite phase on the exit surface during and after hydrogen charging (Figs. 5 and 6) were similar to the potential behavior in the δ-ferrite phase on the entry surface, during and after hydrogen charging (Figs. 3 and 4). Therefore, it is reasonable to consider that the relative decrease of the surface potential in the δ-ferrite phases during charging was attributable to the permeated hydrogen on the exit surface. This preferential detection of permeated hydrogen in the δ-ferrite phases is plausible because the hydrogen diffusion coefficient of the ferrite phase is orders of magnitude larger than that of the austenite matrix at room temperature. In contrast to the behavior of the invaded hydrogen on the entry surface, the delay in the potential recovery was not clearly detected at the boundaries of the δ-ferrite phases on the exit surface after hydrogen charging [Fig. 4(e) and (f)]. This indicates less substantial segregation of permeated hydrogen at the boundaries of the δ-ferrite phases on the exit surface, which implies that the HE mechanism of the material may differ between the outermost surface and the interior for weld metals.

Although the concentration of the permeated hydrogen detected on the exit surface cannot be evaluated in the SKPFM measurements, it has been quantitatively estimated by using the electrochemical method for the permeated hydrogen current density [23, 24]. Furthermore, Akiyama and Li [23] noted that the hydrogen concentration in a carbon steel estimated from the hydrogen permeation current density was in good agreement with the concentration of diffusible hydrogen experimentally measured by thermal desorption analysis (TDA) for the steel. Table 2 shows the experimental results of the hydrogen concentration by the electrochemical method and TDA in ferritic phases for pure iron as well as carbon steels cathodically charged in 0.1 M NaOH [23–26]. Although the material and charging conditions in the present

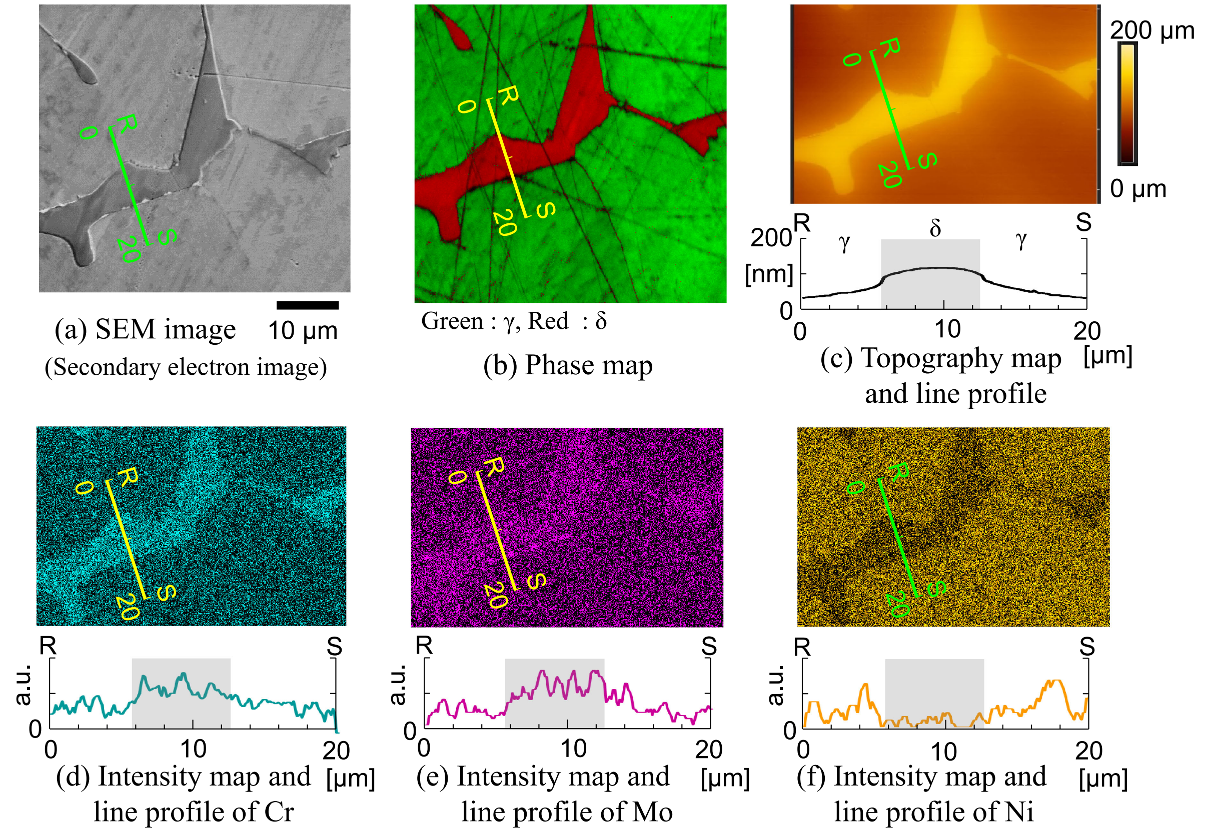

(a) SEM image (Secondary electron image)

(b) Phase map

(c) Topography map and line profile

(d) Intensity map and line profile of Cr

(e) Intensity map and line profile of Mo

(f) Intensity map and line profile of Ni

Fig. 5 (a) SEM image; (b) Phase map; (c) Topography map along R–S line; as well as (d)–(f) Intensity maps along R–S lines of Cr, Mo, and Ni, respectively, in area B on the exit surface.

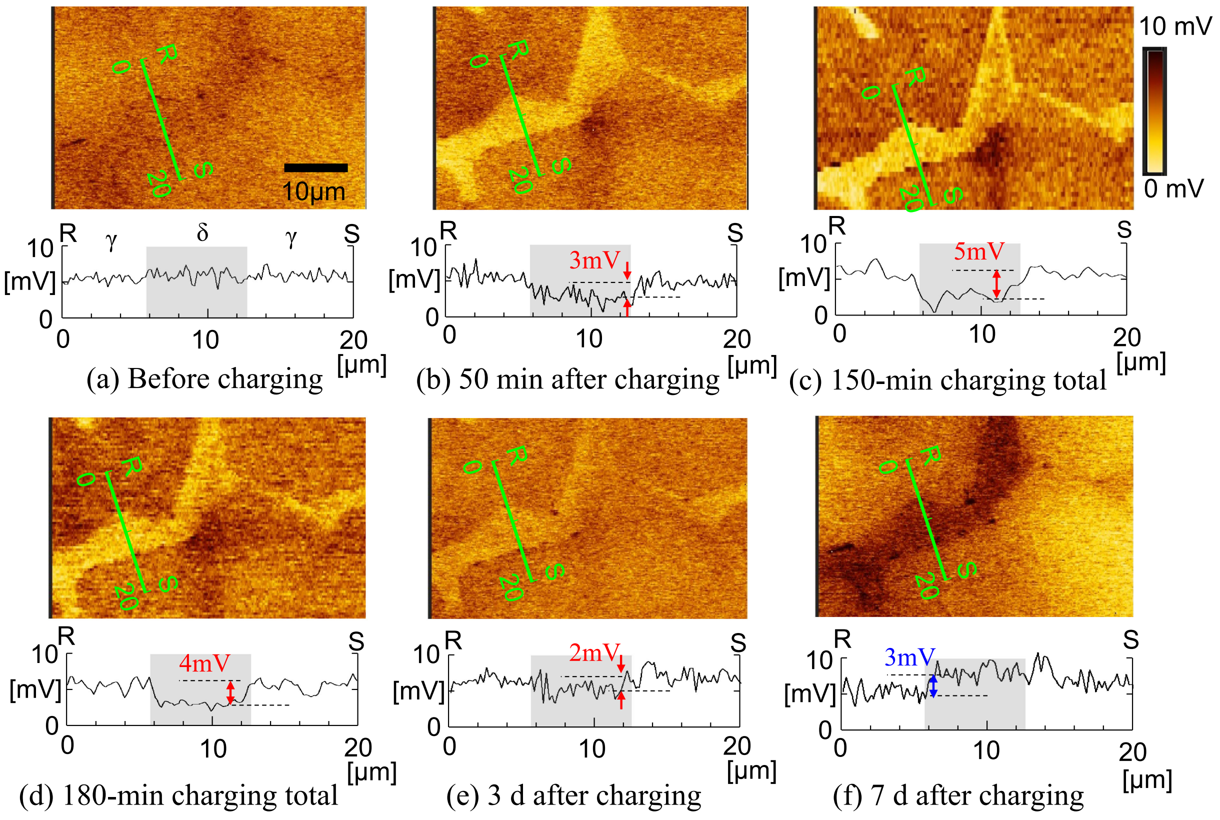

(a) Before charging

(b) 50 min after charging

(c) 150-min charging total

(d) 180-min charging total

(e) 3 d after charging

(f) 7 d after charging

Fig. 6 Potential maps along the P–Q lines in area B: (a) Before charging, (b) 50-min charging, (c) 150-min charging total, (d) 180-min charging total, (e) 3 d after charging, and (f) 7 d after charging.

Table 2 Hydrogen concentration of iron and carbon steel cathodically charged in 0.1 M NaOH by the electrochemical method and TDA.

| Material | Specimen size | Charging current (mA/cm2) | Charging time (hour) | Measureing method | Hydrogen concentration (mass ppm) | Reference |
|---|---|---|---|---|---|---|
| pure iron | 25 mmΦ × 0.5 mm | 2 | 6 | Electrochemical method | 0.5 | [23] |
| AISI 4135 steel | 10 mmΦ × 14 mm | 0.3 | 72 | TDA | 0.5 | [22] |
| AISI 4135 steel | 10 mmΦ × 80 mm | 0.3 | 48 | TDA | 0.34 | [24] |
| AISI 4135 steel | 10 mmΦ × 80 mm | 3 | 72 | TDA | 1.5 | [25] |

experiments did not match those in Table 2, it would be roughly estimated for hydrogen concentrations ranging from 0.1 ppm to several mass parts per million in the δ-ferrite phases when the charging time reaches a steady state of hydrogen permeation. Because the concentration of the permeated hydrogen during 3-h charging in the present experiments must be even smaller than those estimated in Table 2, the present SKPFM measurements under atmospheric pressure could detect at least a 0.1 mass ppm order of hydrogen concentration in the δ-ferrite phases on the exit surface.

### 3.3 Dependence of permeated hydrogen on the microstructure

Multimodal (EBSD, EDS and SKPFM) measurements were also conducted in area C on the exit surface. Figure 7 shows the following: SEM image (Secondary electron image) [Fig. 7(a)]; phase map [Fig. 7(b)]; topography map along the T–U line [Fig. 7(c)]; and intensity maps along the T–U lines of Cr, Mo, and Ni [Fig. 7(d)–(f), respectively] on the exit surface in area C. Spots 1 and 2 were designated in area C [Fig. 7(a)]. Some precipitates formed at the boundary between the δ-ferrite and γ phases, and line segment T–U (length: 8 μm) was set across the precipitates at spot 1. At the precipitates, an approximately 10-nm higher topography [Fig. 7(c)] as well as higher intensities of Cr and Mo—yet little difference in the intensity of Ni—were detected [Fig. 7(d)–(f)]. Regarding the δ-ferrite phase at spot 2, the intensities of Cr, Mo, and Ni were similar to those of the δ-ferrite phases surrounding the spot [Fig. 7(d)–(f)]. Figure 8 shows potential maps along the T–U lines in area C: before charging [Fig. 8(a)], 50-min charging [Fig. 8(b)], 150-min charging [Fig. 8(c)], 180-min charging [Fig. 8(d)], 3 d after charging [Fig. 8(e)], and 7 d after charging [Fig. 8(f)]. The potential of the precipitates in spot 1 was consistently 4- to 5-mV higher than that of the adjacent γ phase (Fig. 8), regardless of hydrogen charging. The potential of the δ-ferrite phase adjacent to the precipitates was almost the same as that of the surrounding δ-ferrite phases in spot 1 before charging [Fig. 8(a)] as well as for 3 and 7 d after charging [Fig. 8(e) and (f)]; however, it was lower by 3, 3, and 4 mV for 50-min charging [Fig. 8(b)], 150-min charging total [Fig. 8(c)], and 180-min charging total [Fig. 8(d)], respectively. Regarding the δ-ferrite phase in spot 2, little variations of the potential relative to that of the surrounding γ phases were detected regardless of hydrogen charging (Fig. 8).

Various intermetallic precipitates are generated during the FA mode solidification of 300 series austenitic stainless steel containing Cr and Mo [4]. These precipitates most frequently contain the sigma (σ) phase, which is an intermetallic compound with the Fe(CrMo) composition and also the intermediate chi (χ) phase because of its Mo rich for SUS316 in the process, leading to formation of the σ phase [4]. A higher surface potential in the σ phase than that of the surrounding austenite matrix has been detected in SKPFM measurements for aging stainless steels [27]. The hydrogen diffusion coefficient of the σ phase has been estimated as lower than that of the ferrite phases [28, 29]. In the present multimodal measurements in spot 1 of area C on the exit surface (Figs. 7 and 8), the surface potential of the precipitate enriched with Cr and Mo was higher than that of the surrounding phases, regardless of hydrogen charging. Because it is assumed that the surface potential of the precipitates was intrinsically higher and that hydrogen was negligibly permeated through the precipitates, the precipitates in spot 1 would contain σ phases. The further decrease in potential during charging [Fig. 8(b) and (c)] in the δ-ferrite phase adjacent to the precipitates strongly implies the effect of accumulating hydrogen on the precipitates. Although some studies have mentioned dissolution of hydrogen into the σ phases [28, 29], the effect of accumulating hydrogen has been reported not at interfaces of σ phases but the intermediate χ phases [4]. Therefore, the intermediate χ phases evidently also included in precipitates in spot 1, and only some precipitates containing the χ phases would have the effect of accumulating hydrogen. Regarding the δ-ferrite phase in spot 2, little variation of the potential regardless of hydrogen charging [Fig. 8(a)–(f)] indicates the absence of permeated hydrogen. Although the δ-ferrite phase in spot 2 was connected with the surrounding δ-ferrite phases where permeated hydrogen was detected, the permeated hydrogen evidently escaped into the air before diffusing to the δ-ferrite phases in spot 2 on the exit surface. Regarding the columnar crystal specimen used in the present experiments, the enlarged phase map of the cross section in Fig. 1(e) implies the presence of discontinuous δ-ferrite phases between the entry and exit surfaces. Because the permeated hydrogen passed through the δ-ferrite phase, the absence of permeated

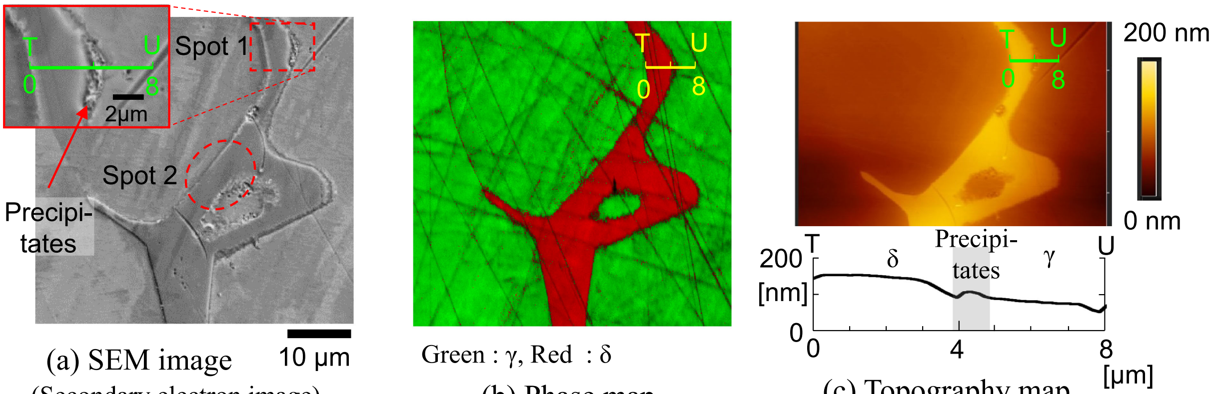

(a) SEM image (Secondary electron image)

(b) Phase map

(c) Topography map and line (T–U) profile

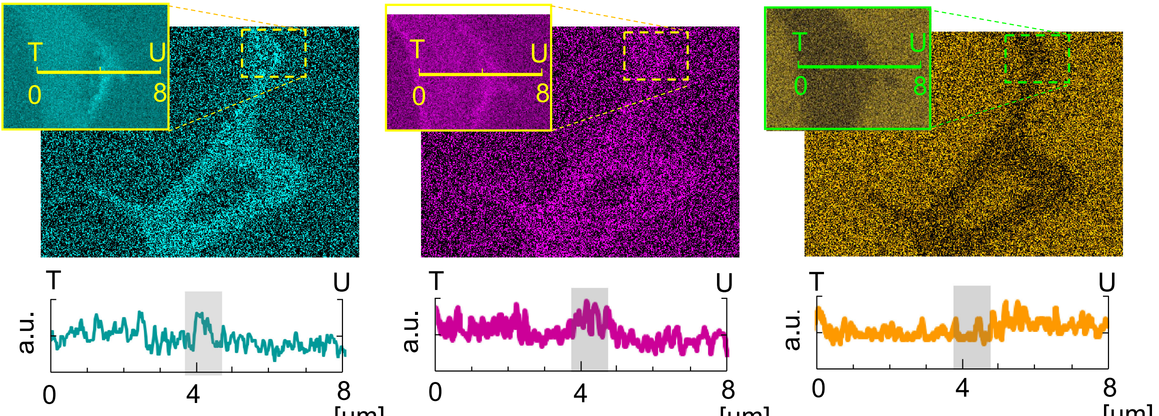

(d) Intensity map and line (T–U) profile of Cr

(e) Intensity map and line (T–U) profile of Mo

(f) Intensity map and line (T–U) profile of Ni

Fig. 7 (a) SEM image; (b) Phase map; (c) Topography map along T–U line; as well as (d)–(f) Intensity maps along T–U lines of Cr, Mo, and Ni, respectively, in area C on the exit surface.

hydrogen in the δ-ferrite phase in spot 2 was attributed to the spatial structures of the δ-ferrite phases between the entry and exit surfaces. The δ-ferrite phase has the function of increasing the sensitivity of HE for weld metals by increasing the hydrogen concentration inside the material [30]. Therefore, the mechanism of HE inside weld metals is closely related to not only hydrogen segregation by precipitates but also internal microstructures, such as spatial structures of the δ-ferrite phases.

Monitoring of invaded/permeated hydrogen based on heterogeneous microstructures by using SKPFM could thus provide important suggestions related to the difference in HE mechanisms between the outermost surface and the interior of weld metals. Because HE of weld metals for austenitic stainless steels has been reported to occur at several mass parts per million of hydrogen concentration [31, 32], SKPFM measurements even under atmospheric pressure are one of the most effective methods for researching HE of weld metals. In welded joints operated in practical environments, the complexity of the internal structures because of the welding histories, as well as the possible further heterogeneous structures such as strain-induced martensitic phases because of the operation histories, is pertinent to the HE mechanism. Further extensive accumulation of experimental data with hydrogen monitoring technology is dispensable for elucidating the mechanism of HE in weld metals.

## 4. Conclusion

The time-sequential distribution of the surface potential on the entry/exit surfaces of cathodically charged SUS316 columnar crystal specimens was evaluated by SKPFM under atmospheric pressure. Columnar crystal specimens were prepared without Pd coating on the surfaces. The microstructures on the entry/exit surfaces were also evaluated by EBSD and EDS in the same areas of the SKPFM measurements. The following conclusions can be drawn.

(1) Invaded hydrogen on the entry surface was detected at the δ-ferrite phases during and after charging, and segregation of invaded hydrogen was emphasized at the boundaries between the δ-ferrite as well as austenite matrix after charging.

(2) Permeated hydrogen on the exit surface was detected at the δ-ferrite phases during and after charging, but not at some of them regardless of the hydrogen charging. Segregation of permeated hydrogen was detected at the boundaries between the δ-ferrite and some of the intermetallic precipitates after charging.

(3) In contrast to preferential initiation of HE at the boundaries between δ-ferrite and the austenite matrix on the surface, the mechanism of HE inside weld metals is closely related to not only hydrogen segregation by

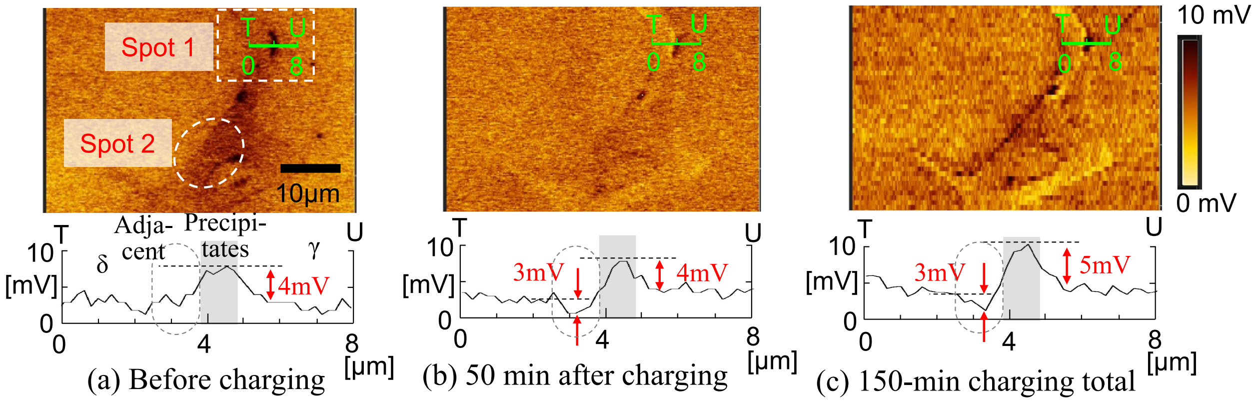

(a) Before charging (b) 50 min after charging (c) 150-min charging total

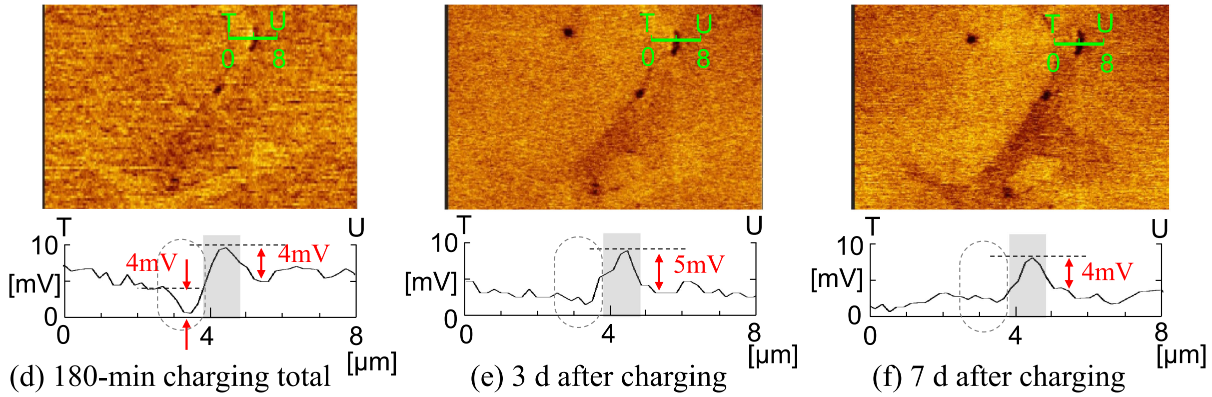

(d) 180-min charging total (e) 3 d after charging (f) 7 d after charging

Fig. 8 Potential maps along the T–U lines in area C: (a) Before charging, (b) 50-min charging, (c) 150-min charging total, (d) 180-min charging total, (e) 3 d after charging, and (f) 7 d after charging.

precipitates but also the spatial structures of the δ-ferrite phases.

(4) SKPFM measurements under atmospheric pressure might facilitate HE research of weld metals even when their surfaces are covered with oxide films.

## REFERENCES

[1] H. Jackson, K. Nibur, C. San Marchi, J. Puskar and B. Somerday: Hydrogen-assisted crack propagation in 304L/308L and 21Cr–6Ni–9Mn/308L austenitic stainless steel fusion welds, Corros. Sci. **60** (2012) 136–144.

[2] N.R. Moody, S.L. Robinson and W.M. Garrison, Jr.: Hydrogen effects on the properties and fracture modes of iron-based alloys, Res. Mechanica **30** (1990) 143–206.

[3] B.P. Somerday, M. Dadfarnia, D.K. Balch, K.A. Nibur, C.H. Cadden and P. Sofronis: Hydrogen-Assisted Crack Propagation in Austenitic Stainless Steel Fusion Welds, Metall. Mater. Trans. A **40** (2009) 2350–2362.

[4] M. Miranda, B. Campillo, J. Colín, A. Torres-_Islas, A. Molina, S. Serna and J.C. Villalobos: Analysis of Electrochemical Hydrogen Permeation through AISI Stainless and Welding Zones for Hydrogen Service, Int. J. Electrochem. Sci. **11** (2016) 9340–9354.

[5] P. Schmutz and G.S. Frankel: Characterization of AA2024-T3 by Scanning Kelvin Probe Force Microscopy, J. Electrochem. Soc. **145** (1998) 2285–2295.

[6] W. Melitz, J. Shena, A.C. Kummela and S. Lee: Kelvin probe force microscopy and its application, Surf. Sci. Rep. **66** (2011) 1–27.

[7] C. Örnek, C. Leygraf and J. Pan: On the Volta potential measured by SKPFM – fundamental and practical aspects with relevance to corrosion science, Corros. Eng. Sci. Technol. **54** (2019) 185–198.

[8] J. Shang and Z. Hua: Hydrogen distribution and segregation in hydrogen-charged S30408 after fracture analyzed via scanning Kelvin probe force microscopy, Appl. Surf. Sci. **528** (2020) 147050.

[9] M. Koyama, M. Rohwerder, C. Tasan, A. Bashir, E. Akiyama, K. Takai, D. Raabe and K. Tsuzaki: Recent progress in microstructural hydrogen mapping in steels: Quantification, kinetic analysis, and multi-scale characterisation, Mater. Sci. Technol. **33** (2017) 1481–1496.

[10] J. Yao, Z. Qi and C. Dong: Real-time evolution and characterization of passive films on individual ferrite and austenite phases of duplex stainless steel, Electrochem. Commun. **137** (2022) 107265.

[11] E. Rahimi, A. Kosari, S. Hosseinpour, A. Davoodi, H. Zandbergen and J.M.C. Mol: Characterization of the passive layer on ferrite and austenite phases of super duplex stainless steel, Appl. Surf. Sci. **496** (2019) 143634.

[12] S. Evers, C. Senoz and M. Rohwerder: Hydrogen detection in metals: a review and introduction of a Kelvin probe approach, Sci. Technol. Adv. Mater. **14** (2013) 014201.

[13] C. Senos, S. Evers, M. Stratmann and M. Rohwerder: Scanning Kelvin Probe as a highly sensitive tool for detecting hydrogen permeation with high local resolution, Electrochem. Commun. **13** (2011) 1542–1545.

[14] G. Wang, Y. Yuan, J. Li, J. Huang and L. Qiao: Investigation of hydrogen evolution and enrichment by scanning Kelvin probe force microscopy, Electrochem. Commun. **35** (2013) 100–103.

[15] G. Wang, Y. Yuan, J. Li, J. Huang, L. Qiao and A. Volinsky: Microstructure effect on hydrogen-induced cracking in TM210 maraging steel, Mater. Sci. Eng. A **586** (2013) 142–148.

[16] S. Evers, C. Senos and M. Rohwerder: Spatially resolved high sensitive measurement of hydrogen permeation by scanning Kelvin probe microscopy, Electrochim. Acta **110** (2013) 534–538.

[17] M. Koyama, A. Bashir, M. Rohwerder, S. Merzlikin, E. Akiyama, K. Tsuzaki and D. Raabe: Spatially and Kinetically Resolved Mapping of Hydrogen in a Twinning-Induced Plasticity Steel by Use of Scanning Kelvin Probe Force Microscopy, J. Electrochem. Soc. **162** (2015) C638–C647.

[18] T. Rubben, K. Baert, T. Depover, K. Verbeken, R. Revilla and I. Graeve: Influence of Thermal Oxide Layers on the Hydrogen Transport through the Surface of SAE 1010 Steel, J. Electrochem.

Soc. **169** (2022) 111503.

[19] H. Inoue, T. Koseki, S. Okita and M. Fuji: Formation mechanism of vermicular and lacy ferrite in austenitic stainless steel weld metals, Sci. Technol. Weld. Joining **5** (2000) 385–396.

[20] Y. Murase, H. Masuda and H. Katayama: Corrosion Resistance of Finer/Coarser Pearlitic Structures of Carbon Steel, J. Electrochem. Soc. **168** (2021) 041501.

[21] M. Luppo, A. Hazarabedian and J. Garcia: Effects of delta ferrite on hydrogen embrittlement of austenitic stainless steel welds, Corros. Sci. **41** (1999) 87–103.

[22] B.R.S. da Silvia, F. Salvio and D.S. dos Santos: Hydrogen induced stress cracking in UNS S32750 super duplex stainless steel tube weld joint, Int. J. Hydrogen Energ. **40** (2015) 17091–17101.

[23] E. Akiyama and S. Li: Electrochemical hydrogen permeation tests under galvanostatic hydrogen charging conditions conventionally used for hydrogen embrittlement study, Corros. Rev. **34** (2016) 103–112.

[24] H. Addach, P. Bercot, M. Rezrazi and J. Takadoum: Study of the electrochemical permeation of hydrogen in iron, Corros. Sci. **52** (2009) 263–267.

[25] M. Wang, E. Akiyama and K. Tsuzaki: Crosshead speed dependence of the notch tensile strength of a high strength steel in the presence of hydrogen, Scr. Mater. **53** (2005) 713–718.

[26] Y. Hagiwara, C. Ito, N. Hisamori, H. Suzuki, K. Takai and E. Akiyama: Evaluation of Delayed Fracture Characteristics of High Strength Steel based on CSRT Method, Tetsu-to-Hagané **94** (2008) 215–221.

[27] Y. Honma, G. Sasaki, K. Hashi, H. Masuda, M. Hayakawa and K. Nagai: Application of Kelvin Probe Force Microscopy to Microstructure Evaluation of Steel, Tetsu-to-Hagané **106** (2020) 39–49.

[28] L. Fernandes, L. Claeys, M. Pinson, T. Depover, D. Santos and K. Verbeken: Evaluating the Hydrogen Embrittlement Susceptibility of Aged 2205 Duplex Stainless Steel Containing Brittle Sigma Phase, Steel Res. Int. **92** (2021) 2000693.

[29] T. Kuroda and K. Nakade: Behavior of Hydrogen in Super Duplex Stainless Steels, Trans. JWRI **37** (2008) 73–78.

[30] C. Hempel, M. Mandel, C. Quitzke, M. Radajewski, C. Schröder, M. Wendler, O. Volkova and L. Kruger: Hydrogen Embrittlement in a Plasma Tungsten Inert Gas-Welded Austenitic CrMnNi Stainless Steel, Steel Res. Int. **94** (2023) 2200870.

[31] I.M. Robertson, P. Sofronis, A. Nagao, M.L. Martin, S. Wang, D.W. Gross and K.E. Nygren: Hydrogen Embrittlement Understood, Metall. Mater. Trans. B **46** (2015) 1085–1103.

[32] R. Silverstein and D. Eliezer: Mechanisms of hydrogen trapping in austenitic, duplex, and super martensitic stainless steels, J. Alloy. Compd. **720** (2017) 451–459.